Self-Biased Hybrid Piezoelectric-Photoelectrochemical Cell with Photocatalytic Functionalities

Chuan Fu Tan,[||,†] Wei Li Ong,[||,‡] and Ghim Wei Ho*[,†,‡,§]

[†]Engineering Science Programme, National University of Singapore, 9 Engineering Drive 1, Singapore 117575, [‡]Department of Electrical and Computer Engineering, National University of Singapore, 4 Engineering Drive 3, Singapore 117583, and [§]Institute of Materials Research and Engineering, A*STAR (Agency for Science, Technology, and Research), 3 Research Link, Singapore 117602. [||]These authors contributed equally.

ABSTRACT Utilizing solar energy for environmental and energy remediations based on photocatalytic hydrogen (H_2) generation and water cleaning poses great challenges due to inadequate visible-light power conversion, high recombination rate, and intermittent availability of solar energy. Here, we report an energy-harvesting technology that utilizes multiple energy sources for development of sustainable operation of dual photocatalytic reactions. The fabricated hybrid cell combines energy harvesting from light and vibration to run a power-free photocatalytic process that exploits novel metal—semiconductor branched heterostructure (BHS) of its visible light absorption, high charge-separation efficiency, and piezoelectric properties to overcome the aforementioned challenges. The desirable characteristics of conductive flexible piezoelectrode in conjunction with pronounced light scattering of hierarchical structure originate intrinsically from the elaborate design yet facile synthesis of BHS. This self-powered photocatalysis system could potentially be used as H_2 generator and water treatment system to produce clean energy and water resources.

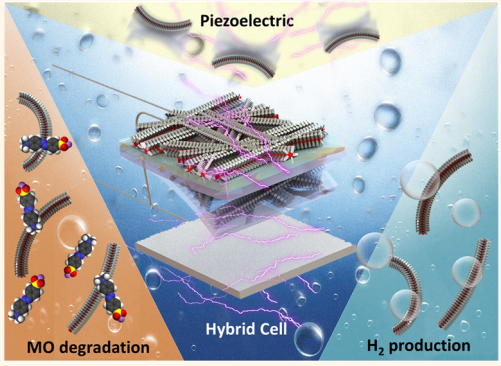

KEYWORDS: piezoelectric · photoelectrochemical · photocatalyst · zinc oxide · metal sulfide · heterostructure · solar hydrogen

The rapid depletion of natural energy resources coupled with the worsening environmental pollution issues call for the need to develop sustainable energy-conversion technologies relying on alternative resources. However, in all these individual energy harvesting technologies, other forms of associated energies are usually not tapped and hence wasted. Due to the unpredictable availability of renewable energy sources, it is desirable to create a hybrid device that captures power from multiple sources.[1−4] Among the various renewable energy resources, mechanical vibrations[5] and solar power[6] are two of such sources of energy that are readily available and easily accessible which can be tapped by nanogenerators[7−13] and photoelectrochemical (PEC)[14−17] cells, respectively. Moreover, both mechanical and solar energy can also initiate H_2 generation[18,19] and water pollutants degradation[20−22] by piezopotential and photocatalysis processes which are of great significance for environmental remediation and renewable energy production. Despite the fascination and compelling benefits of fabricating a multiple-energy-sources powered system for integrated photocatalysis functionalities, realization of such device is unprecedented due to various material incompatibility and fabrication challenges. Hence, it is of utmost importance to develop viable fabrication processes that encompass performance and cost trade-offs which have limited large-scale applications of such self-powered multifunctional device.

Zinc oxide (ZnO) is highly regarded for its piezoelectric properties due to its noncentrosymmetric lattice structure,[23] making it an ideal material for piezoelectric nanogenerators.[24−30] However, as a photocatalyst, it offers mediocre performance due to high recombination rates and is only functional within the ultraviolet (UV) spectrum due to its wide bandgap.[31] Moreover, one-dimensional nanostructure remains the most widely used nanostructure for piezo-nanogenerator and PEC devices simply because fabrication of

* Address correspondence to elehgw@nus.edu.sg.

Received for review May 21, 2015 and accepted June 29, 2015.

Published online June 29, 2015
10.1021/acsnano.5b03075

hierarchical nanostructured device is both complex and formidable. However, it is well-known that elaborate nanostructure engineering promises new opportunities and could drastically improve the energy conversion performance. In this regard, hierarchical nanostructures of diverse material compositions are attractive due to their appealing attributes of long optical paths for efficient light absorption, optimized interfaces for visible light activation, high-quality conducting media for rapid electron–hole separation and charge transport as well as high surface areas for fast interfacial charge transfer and electrochemical reactions. Hence, a departure from the conventional paradigm of one-dimensional planar device along with dedication in designing materials composition and structural architecture to promote energy conversion efficiency is highly desirable.

In this paper, we report a multiple-energy-source powered PEC system based on a unique metal–semiconductor BHS. A novel seedless galvanic displacement method was employed to aid in designing complex hierarchical nanostructures of diverse material compositions at low processing requirements. A complementary approach of partially encapsulating BHS in polydimethylsiloxane (PDMS) for piezoelectric harvesting while the exposed BHS undergoes facile sulfurization was proposed for integration of vibrational and solar energy conversion jointly with photocatalysis functionalities on an integral monolithic platform. The sulfurized BHS aims to overcome the previously mentioned drawbacks of ZnO material as photocatalyst,[32] and at the same time, the sulfurized core metallic nanowires (NWs) serve as co-catalyst, thereby offering higher charge-separation efficiency and photosensitivity toward visible light. The synergistic features of conductive flexible piezoelectrode and favorable light manipulation[33] are exhibited by the elaborate design of BHS. This two-in-one mechanically flexible hybrid cell combines piezoelectricity and photoelectrochemistry to harvest mechanical and light energy, respectively. A self-bias function of the piezoelectric-photoelectrochemical hybrid cell is also demonstrated together with the photocatalytic splitting of water and degradation of polluted water.

RESULTS AND DISCUSSION

Large quantities of silver (Ag) and copper (Cu) NWs with uniform diameters of 100 nm and lengths ranging from 5 to 20 μm (Supporting Information Figure S1) were synthesized by the hydrothermal method. The Ag NWs fabricated by the PVP-assisted polyol reduction method were reported to possess a pentagonal cross-section with five-fold symmetry.[34] The ends of the NWs are terminated by {111} facets, while the side surfaces are bounded by five {100} facets. The {100} facets are passivated by PVP, resulting in the occurrence of growth predominantly along the {111} facets. The multiple twin-induced pentagonal geometry of Ag NWs is a stable structure produced by chemical growth methods. On the other hand, Cu NWs had a penta-twinned structure bounded by 10 {111} facets at the two ends and five {100} side face as well.[35] ZnO nanorods (NRs) were then grown on the Ag and Cu NWs via a galvanic displacement deposition method, and a highly directional growth of ZnO NRs was observed along the length of the metallic NWs (Figure 1a,b,f,g). The growth of ZnO NRs was observed across the entire network of metallic NWs, indicating the presence of good contacts between the metallic NWs, which facilitate charge transfer for the galvanic deposition process.

The galvanic deposition method of growing ZnO NRs is a contact potential driven process, as shown in Figure 1m.[36] A potential bias generated from the work function difference between the metallic NWs cathode and aluminum (Al) foil sacrificial anode drives the reactions shown in Figure 1m. Since the reduction potential for Al is more negative than that of the cathode, electrons will flow from Al to the metallic NWs, generating a positive charge on Al (reaction 1). A reduction reaction of dissolved oxygen occurs on the cathodic metallic NWs substrate to produce OH^- ions (reaction 2). The Zn^{2+} ions in the electrolyte then react with the OH^- ions to form $Zn(OH)_2$ on the metallic NWs, which subsequently dehydrates to form ZnO NRs.

$$\text{At the Al anode : } Al \rightarrow Al^{3+} + 3e^- \quad (1)$$

$$\text{At the metallic NWs cathode : } O_2 + 2H_2O + 4e^- \rightarrow 4OH^- \quad (2)$$

$$Zn(OH)_2 \rightarrow ZnO + H_2O$$

The galvanic deposition of ZnO on the facets of the Ag NWs creates a well-defined five-sided growth morphology, as illustrated in Figure 1m. A less directed growth of ZnO NRs was observed on Cu NWs, probably due to the existence of a thin copper oxide layer, which has influenced the lattice matching and the charge transfer of the galvanic deposition process.

The Ag-ZnO (AZ) and Cu-ZnO (CZ) BHS were then sulfurized and the high-resolution transmission electron microscopy (HRTEM) images of the NRs are shown in Figure 1k,m. A core–shell structure is observed; with the lattice spacing of the shell being different from that of the core, indicating the presence of two different materials. The core is identified as ZnO with a lattice spacing of 0.26 nm, while the shell consists of ZnS nanoparticles with a lattice spacing of 0.31 nm.[37] This suggests that during the sulfurization process, ZnS was formed as an outer shell layer, while the inner core remained as ZnO, producing a core–shell structure as reported by Kushwaha et al.[38] The crystallinity of the Ag/Ag_2S-ZnO/ZnS (ASZS) and Cu/CuS-ZnO/ZnS (CSZS)

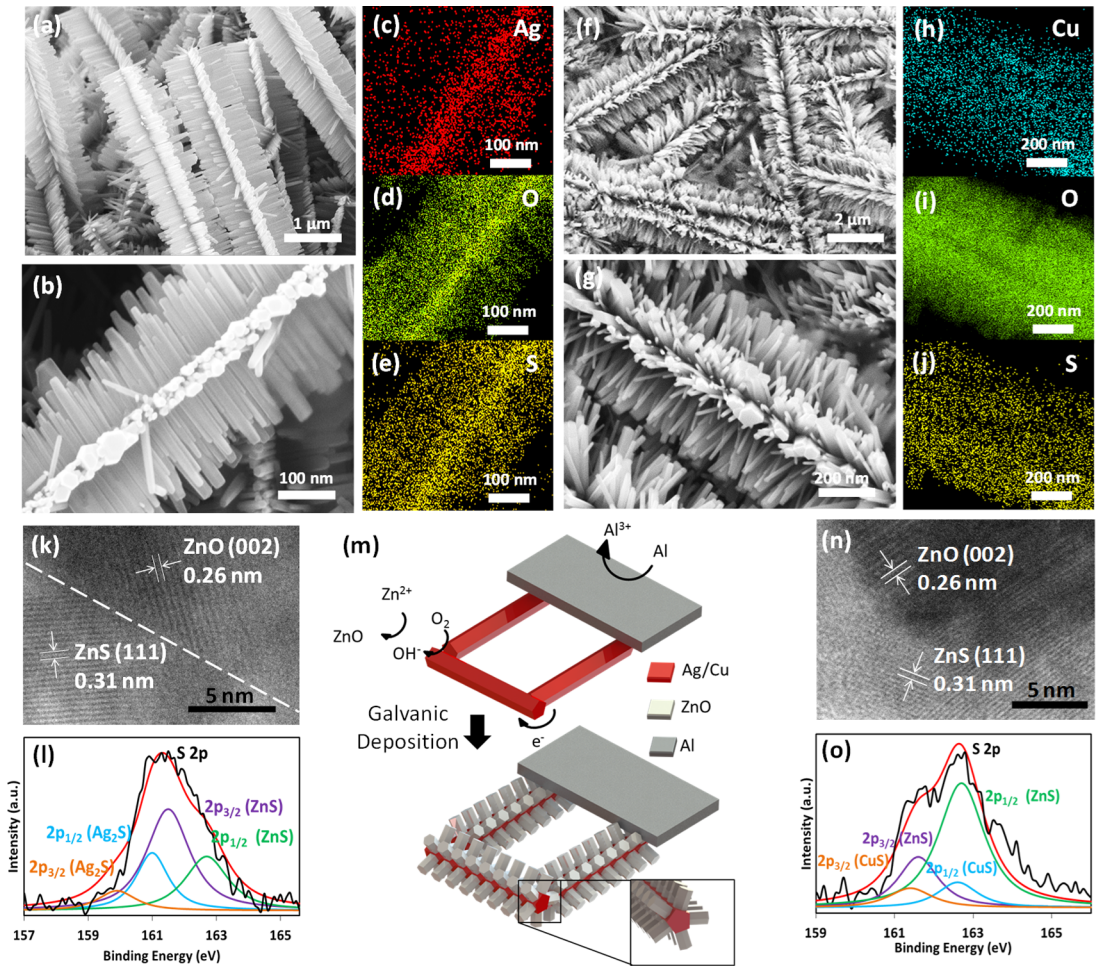

Figure 1. SEM images of (a,b) AZ and (f,g) CZ with corresponding elemental mapping (c,d,e) and (h,i,j). (m) Schematic illustration of the galvanic cell deposition mechanism in the formation of BHS structure. HRTEM images of (k) ASZS and (n) CSZS and XPS spectra of (l) ASZS and (o) CSZS, respectively.

BHS was also characterized by X-ray diffraction (XRD) (Supporting Information Figure S3), and presence of the diffraction planes corresponding to the various materials indicates that the sulfurization process was successful. The elemental composition of the sulfurized heterostructure was further investigated in scanning transmission electron microscopy (STEM). The elemental maps in Figure 1c–e show the distribution of Ag, O and S on a ASZS BHS. It can be seen that Ag is concentrated in the core of the BHS (Figure 1c), while S is observed to have diffused uniformly across the entire BHS (Figure 1e), suggesting that the sulfurization process was successful in producing ZnS and Ag_2S. Elemental mapping was also carried out on an individual ZnO/ZnS (ZS) NR (Supporting Information Figure S4). The presence of S is detected along with O, but the distinction between the ZnS outer shell and ZnO core depicted in the HRTEM images could not be made from the elemental maps. This could be due to hybridization of the ZnS outer shell with the ZnO core. Elemental mapping was also carried out on the CSZS BHS (Figure 1h–j), and a similar observation was made. The S element was observed to be uniformly distributed across the BHS, indicating that both the ZnO NRs and Cu NWs were sulfurized.

X-ray photoelectron spectroscopy (XPS) was carried out to determine the valence states of the elements present in ASZS (Supporting Information Figure S5) and CSZS (Supporting Information Figure S6). The peaks at 368.3 and 374.3 eV are assigned to the binding energies of Ag $3d_{5/2}$ and Ag $3d_{3/2}$ from Ag^0 metal[39] (Supporting Information Figure S5a), while the 368.8 and 374.8 eV peaks represent the binding energies of Ag $3d_{5/2}$ and Ag $3d_{3/2}$ from Ag^+ in Ag_2S.[39] Zn and O peaks were also detected as shown in Supporting Information Figure S5b,c, respectively. The Zn $2p_{3/2}$ peak can be deconvoluted into 2 peaks at 1021.7 and 1022.4 eV, which can be attributed to Zn–S and Zn–O, respectively.[40] Deconvolution of the O 1s peak revealed two peaks centered at 530.1 and 531.2 eV. The peak at 530.1 eV can be attributed to Zn–O, while the peak at 531.2 eV is ascribed to the chemisorbed oxygen caused by the surface hydroxyl groups, which corresponds to the O–H bonds.[41] The S 2p spectrum (Figure 1l) is best fitted with two doublets, and the doublet at the higher binding energies of 161.6 eV

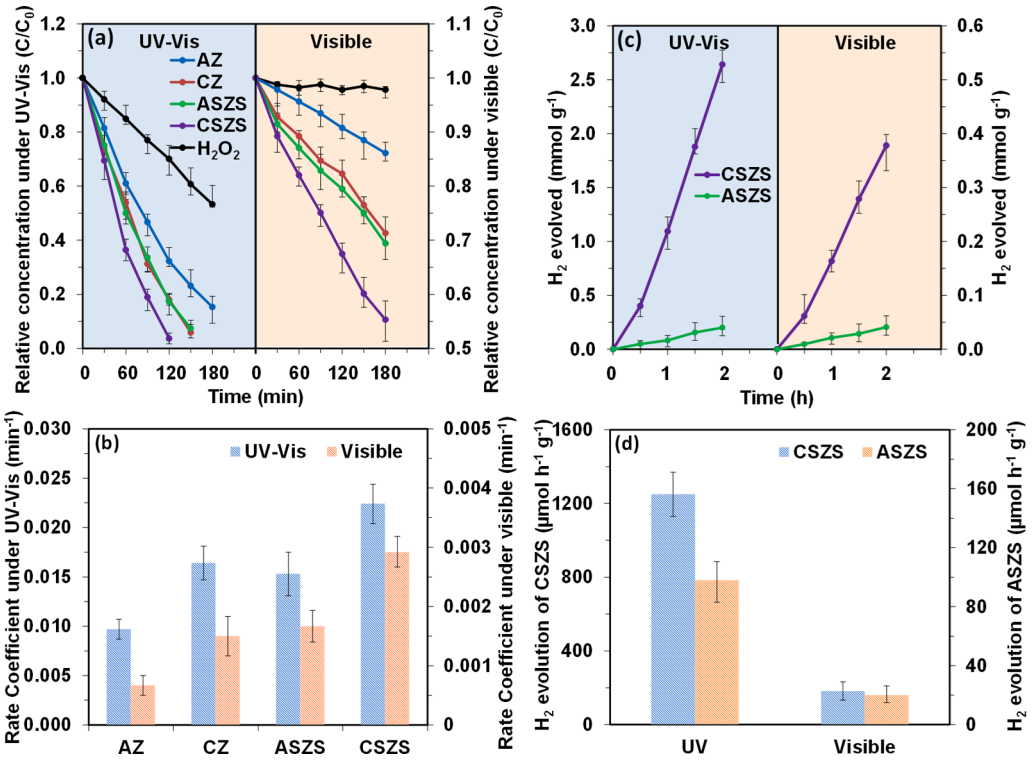

Figure 2. Photodegradation of MO under (a) UV−vis and visible illumination. (b) Rate coefficients of the BHS in degradation of MO. (c) Amount of H_2 evolved from the sulfurized BHS in both UV−vis and visible illumination with (d) corresponding H_2 evolution rates.

(S $2p_{3/2}$) and 162.8 eV (S $2p_{1/2}$) is assigned to the Zn−S bonds,[38] whereas the other at a relatively lower binding energy of 159.8 eV (S $2p_{3/2}$) and 160.9 eV (S $2p_{1/2}$) is in good agreement with the Ag−S bonds.[42] This means that the sulfurized BHS is comprised of Ag, Ag_2S, ZnO, and ZnS. For CSZS BHS, the Cu $2p_{3/2}$ and $2p_{1/2}$ peaks (Supporting Information Figure S6a) at 932.9 and 952.6 eV can be attributed to Cu^0 metal,[43] while the 932.4 and 952.1 eV peaks represent the binding energies of Cu $2p_{3/2}$ and $2p_{1/2}$ of Cu^{2+} in CuS.[44] Similar to the ASZS BHS, the Zn $2p_{3/2}$ peak (Supporting Information Figure S6b) can be deconvoluted into two peaks at 1021.7 and 1022.4 eV, which can be attributed to Zn−S and Zn−O, respectively.[40] Deconvolution of the O 1s peak (Supporting Information Figure S6c) revealed two peaks centered at 530.2 and 531 eV, which can be attributed to Zn−O and chemisorbed oxygen (O−H bonds), respectively.[41] The S 2p spectrum (Figure 1o) can be deconvulated into two doublets, with the doublet of 161.6 eV (S $2p_{3/2}$) and 162.8 eV (S $2p_{1/2}$) being attributed to the Zn−S bonds,[38] while the other doublet of 161.4 eV (S $2p_{3/2}$) and 162.6 eV (S $2p_{1/2}$) is in good agreement with the Cu−S bonds.[45]

The photocatalytic performance of the BHS is shown in Figure 2. The BHS was able to degrade methyl orange (MO) under UV−vis illumination (300 W xenon arc lamp, intensity 100 mW cm^{-2}), with the CSZS BHS exhibiting the best performance of complete degradation in 120 min (Figure 2a). The BHS could also degrade MO in visible illumination (420 nm cutoff filter) but at a slower rate. The pseudo-first-order kinetics of the various photocatalysts were analyzed using the pseudo-first-order model[46] as follows:

$$\ln(C_0/C_t) = kt \quad (3)$$

where C_0 and C_t are the concentrations of MO at time 0 and t, respectively, and k is the pseudo-first-order rate constant. The pseudo-first-order rate constants, k, of the BHS are shown in Figure 2b. The sulfurized BHS performed better than the nonsulfurized BHS, with the Cu-based BHS performing better than the Ag-based BHS. The CSZS BHS showed the highest rate constants k of 0.0224 and 0.0035 min^{-1} in UV−vis and visible irradiation, respectively. It should be noted that without any photocatalysts, the degradation of MO by hydrogen peroxide (H_2O_2) under UV−vis irradiation was relatively slow, while no degradation was observed under visible irradiation. Besides MO degradation, the sulfurized BHS was also capable of producing H_2 from the photocatalytic splitting of water shown in Figure 2c,d. The ASZS BHS produced H_2 at a rate of 98.8 μmol h^{-1} g^{-1} under UV−vis illumination and 20 μmol h^{-1} g^{-1} under visible illumination, as shown in Figure 2d. The CSZS BHS performed much better with a H_2 production rate of 1250 μmol h^{-1} g^{-1} under UV−vis illumination and 182 μmol h^{-1} g^{-1} under visible illumination. A similar trend was observed in the absorbance spectra of the BHS (Supporting Information Figure S7). The sulfurized

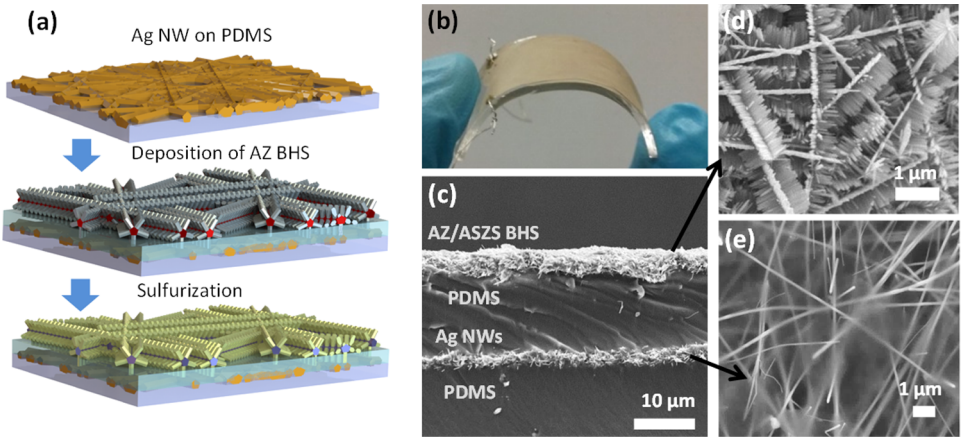

Figure 3. (a) Fabrication procedure of hybrid cell. (b) Photograph of flexible hybrid device with corresponding (c) cross section SEM image. The top active layer of (d) AZ/ASZS and bottom electrode of (e) Ag nanowires are shown.

BHS exhibited increased absorbance across wavelengths 300 to 800 nm compared to nonsulfurized BHS, with the CSZS BHS having the highest absorbance. This shows that sulfurization results in increased light absorption and sensitivity toward visible wavelengths.

Sulfurization of the BHS leads to hybridization between the band structures of oxides and sulfides, as reported by Zhu et al.[47,48] By hybridizing the wide bandgap materials (ZnO and ZnS) with the narrow bandgap materials (Ag_2S or CuS), the resultant bandgap of the composite is reduced and sensitive to visible wavelengths. The elemental maps show the out-diffusion of Ag and Cu to the ZnO NRs in the ASZS and CSZS BHS, indicating the occurrence of hybridization during sulfurization. The process of out-diffusion also aids in optimizing the contact interface for enhanced heterojunction-induced charge transfer[48] from ZS to Ag/Ag_2S (AS) and Cu/CuS (CS). When the BHS is irradiated with UV–vis or visible light, electrons are excited from the valence band to the conduction band to produce H_2 by reduction, while the holes are quenched by the sacrificial reagent (S^{2-}/SO_3^{2-}).[49] The transfer of photogenerated electrons to AS and CS reduces the recombination rate, hence resulting in enhanced photocatalytic performance. In the case of MO degradation, photogenerated electrons react with dissolved oxygen molecules and produce oxygen peroxide radicals (reaction 4), while the positively charged holes react with OH^- and H_2O to form hydroxyl radicals (reactions 5 and 6). These radicals are powerful oxidizing agents capable of degrading MO to CO_2, H_2O, and other mineralization products (reaction 7).[50]

$$e^- + O_2 \rightarrow O_2^{\bullet -} \quad (4)$$

$$h^+ + OH^- \rightarrow OH^{\bullet} \quad (5)$$

$$h^+ + H_2O \rightarrow OH^{\bullet} + H^+ \quad (6)$$

$$O_2^{\bullet -} \text{ or } OH^{\bullet} + MO \rightarrow \text{degradation products} \quad (7)$$

The fabrication of the hybrid device involves separate synthesis of the Ag and AZ electrodes and the process is illustrated in (Figure 3a). The Ag electrode was fabricated by pouring PDMS over the polytetrafluoroethylene (PTFE) membrane supported Ag NWs filtrate and curing at 90 °C for 1 h. After removing the PTFE membrane, the Ag electrode was obtained in the form of a Ag NWs-PDMS matrix layer. The AZ electrode was then fabricated by pouring PDMS on the Ag electrode, followed by placing the AZ BHS (supported on another PTFE membrane) on top, and curing the PDMS at 90 °C for 1 h. After the PDMS has cured, the PTFE membrane was removed, leaving a partial encapsulated and partial exposed AZ BHS layer, which was then sulfurized. SEM images depicting the cross-section, active, and counter electrodes of the hybrid device are shown in Figure 3c–e. The partially exposed AZ BHS layer is shown in Figure 3d and Figure S8 (Supporting Information). The liquid PDMS flows inside the semiporous network of AZ BHS and fills the pores due to capillary forces. However, the penetration of PDMS through the layer is limited by the compactness of the BHS from vacuum filtration, hence resulting in a partial encapsulated layer. The cured PDMS binds the BHS together like a film that is highly flexible, as shown in Figure 3b. To demonstrate the potential applications of the hybrid cell, the piezoelectric voltage output from the hybrid cell was directly applied to the PEC water splitting and MO degradation with UV–vis light irradiation and ultrasonic vibration. The piezoelectric output and PEC photocurrent were first measured separately to understand the performance of the individual components (Figure 4a) before combining them together and measuring the output from the hybrid cell (Figure 4d).

The piezoelectric response of the device subjected to cycles of ultrasonic vibration at 60 s interval is shown in Figure 4b, and a peak-to-peak voltage of 2 V was recorded. The piezoelectric output in subsequent cycles was relatively consistent with minimum decay

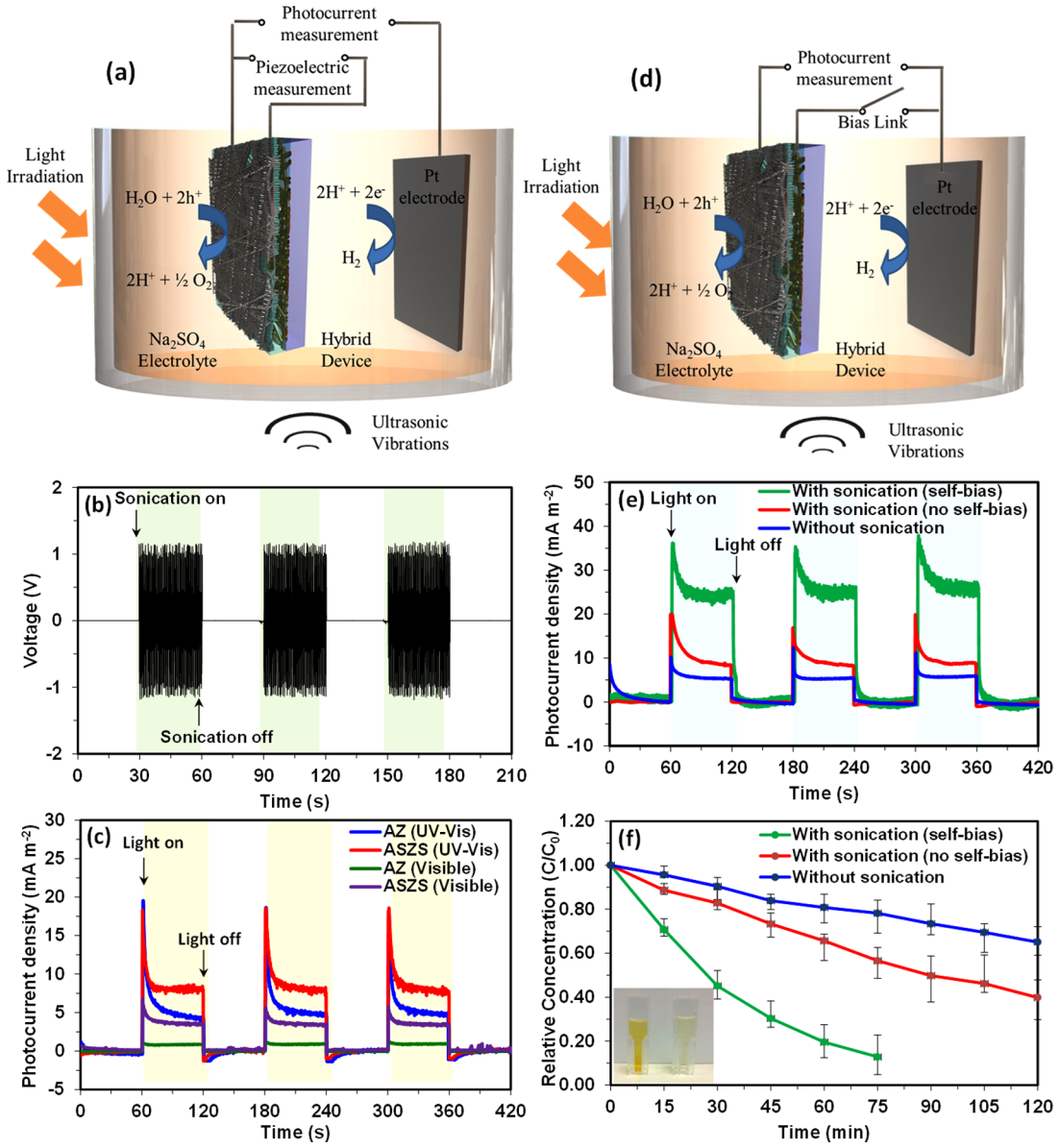

Figure 4. Schematic illustration of (a) individual component measurement of (b) piezoelectric voltage and (c) photocurrent of the hybrid cell. Schematic illustration of (d) self-bias hybrid system via a bias link with the corresponding enhanced (e) photocurrent measurement and (f) MO photodegradation.

due to the encapsulation of the ZnO NRs. When a force normal to the nanogenerator is applied, uniaxial compressive stress is generated. Due to the piezoelectric effect, the tip of the ZnO NRs will have a negative piezoelectric potential, increasing the Fermi level at the tip. The electrons will then flow from the tip to the bottom through the external circuit, generating a positive electrical potential at the tip in the process. The PDMS insulating layer prevents the electrons from being transported directly across to the Ag NWs layer, thereby maintaining the potential at the tip. Inductive charges established at the top and bottom electrodes due to electrostatic forces then go on to flow through an external load. Removal of the force results in the diminishing of the piezopotential, and this releases the stored electrons. The sonicating process would result in a dynamically applied stress on the device, which drives the electrons in the external circuit to flow back and forth, resulting in an alternating output.[51]

The AZ and ASZS active electrodes were tested in a two-electrode PEC configuration with Pt foil as the counter electrode. After three cycles of UV−vis illumination, the ASZS electrode exhibited the highest photocurrent density of about 10 mA m^{-2}, which was twice as large as that of the AZ electrode (Figure 4c). It is believed that the ASZS heterostructure provided considerable synergistic effects toward reduction in energy barrier at the interface, enhancement of charge transport, and improvement in separation efficiency of photogenerated carriers.[52] The ASZS BHS was also photosensitive toward visible light, and

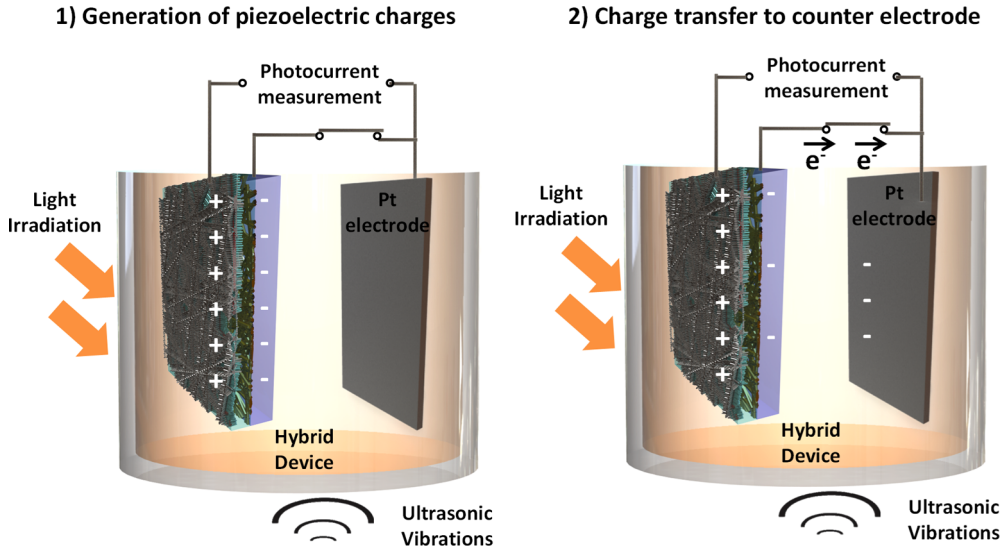

Figure 5. Proposed charge-transfer mechanism between the piezoelectric nanogenerator and photoelectrochemical cell.

a photocurrent of about 5 mA m^{-2} was obtained (Figure 4c). The photogeneration of electron–hole pairs for the PEC experiment is similar to that of the photocatalytic proceses. When the ASZS BHS was illuminated, the photogenerated electrons were transferred to the Ag electrode and then moved toward the Pt counter electrode to reduce water into H_2, while the photogenerated holes were released to the electrolyte solution. The presence of conductive metallic NWS at the core makes the BHS good candidates for PEC electrodes as it negates the need to deposit them on a conductive substrate. Being partially encapsulated in PDMS, the BHS can be easily removed or recycled as compared to the traditional suspension-based photocatalysis. In addition, the one-dimensional components of the BHS allow for a high charge-transfer rate with a large surface area for effective adsorption/desorption of molecules.

The schematics in characterizing the hybrid device under simultaneous UV–vis light irradiation and ultrasonic vibration are shown in Figure 4d. Upon sonication, piezoelectric charges will be generated in the hybrid cell, and charge transfer will occur between the Ag NWs electrode and the Pt counter electrode of the PEC cell. This creates a voltage bias between the active electrode of the hybrid cell and the Pt electrode (Figure 5). The PEC photocurrent density improved from 8 mA m^{-2} to 22 mA m^{-2} when sonication was applied, suggesting that self-biasing due to the piezoelectric effect has led to an increase in the photocurrent measured (Figure 4e). The Ag NWs electrode of the hybrid cell was then disconnected from the PEC Pt counter electrode to determine the amount of improvement in photocurrent due solely to agitation of electrolyte by sonication. The enhancement of the photocurrent was lower, suggesting that the bias from the piezoelectric voltage has a significant effect on the photocurrent. The observed increase in photocurrent with an alternating voltage bias from the piezoelectricity can be attributed to a larger increase in photocurrent density during forward bias and a smaller decrease during reverse bias. This nonsymmetric nature of the current–voltage (I–V) curve in forward and reverse bias is due to the rectification property of semiconductor electrolyte junction.[53]

Besides light energy harvesting and H_2 production, the hybrid cell also serves to enhance PEC degradation of MO. A configuration similar to the photocurrent measurement was used to investigate the degradation rate of the self-biased hybrid cell. Under UV–vis illumination with the self-bias configuration, MO was degraded in 75 min (Figure 4f). This degradation rate is higher than that without self-bias connection and without sonication as shown in Figure 4d. A digital photograph (Figure 4f inset) shows the MO before and after complete degradation. It has been reported that the application of a bias voltage improves the degradation rate[54] due to the enhanced transport of photogenerated charges to the Pt counter electrode, which suppresses recombination of the electrons and holes. Reactions between photoelectrons at the counter electrode and the dissolved oxygen molecules produced $O_2^{\bullet -}$ radicals, which are capable of degrading most pollutants.[55]

CONCLUSIONS

A novel piezoelectric-photoelectrochemcial hybrid device based on BHS has been fabricated and characterized under mechanical vibration and light irradiation. A simple method of growing ZnO NRs on one-dimensional NW conductors is first demonstrated in this work, along with the study of its piezoelectric and photocatalytic properties in the hybrid cell. We have shown that the BHS in the form of

multicomponent structural and material composition is highly promising for enhanced solar energy harvesting and conversion capabilities. This would also pave the way for a new generation of self-powered and flexible photocatalytic devices for environmental and energy science applications.

EXPERIMENTAL SECTION

Synthesis of Ag and Cu NWs. Ag NWs were synthesized via a modified polyrol process, which involved the reduction of silver nitrate ($AgNO_3$) in the presence of polyvinylpyrrolidone (PVP, average mol wt 1,300,000) in ethylene glycol (EG). Two g of iron(III) chloride ($FeCl_3$) solution (6×10^{-4} M in EG), 0.27 g of $AgNO_3$, and 0.1 g of PVP were added to 30 mL of EG. The mixture was stirred for 12 h and then transferred to a Teflon-lined autoclave and heated at 150 °C for 1.5 h. Cu NWs were synthesized following procedures detailed in a previously published work.[56]

Synthesis and Sulfurization of Ag-ZnO (AZ) and Cu-ZnO (CZ) BHS. The synthesized metallic NWs were filtered through a polytetrafluoroethylene (PTFE) membrane filter (Omnipore, pore size 0.2 μm) and rinsed with isopropanol (IPA). Aluminum (Al) foil was adhered to the membrane supported metallic NWs filtrate and then placed in a growth solution containing 25 mM of zinc nitrate hexahydrate ($Zn(NO_3)_2 \cdot 6H_2O$) and 25 mM of hexamethylenetetramine (HMT) in DI water. The solution was maintained at 90 °C for 3 h, and the as-synthesized AZ or CZ BHS was rinsed in ethanol and dried at 55 °C. The BHS was subsequently sulfurized by immersing in 1 M Na_2S solution at 70 °C for 4 h and air-dried after rinsing with IPA.

Photocatalytic Measurement (Water Splitting and Methyl Orange Degradation). Two mg of photocatalysts was dispersed in 10 mL of 0.35 M Na_2S/0.25 M Na_2SO_3 aqueous solution in a 25 mL quartz reaction cell sealed with a rubber septum. The cell was purged with argon (Ar) gas and then irradiated with a 300 W xenon arc lamp (intensity 100 mW cm^{-2}) with magnetic stirring. Gas samples extracted periodically were analyzed with a gas chromatograph to determine the amount of H_2 produced. Photodegradation of methyl orange (MO) was investigated by dispersing 15 mg of photocatalysts in 15 mL of aqueous MO solution (0.04 mM) with 0.1 mL of hydrogen peroxide (H_2O_2) and stirring in the dark for 30 min to attain complete adsorption−desorption equilibrium before illumination. The concentration of MO was determined using a UV−vis-NIR spectrophotometer. The experiments were repeated under visible light irradiation with a 420 nm cutoff filter.

Fabrication of Device. The fabrication process involves separate synthesis of the Ag and AZ electrodes. The Ag electrode was fabricated by pouring PDMS over the PTFE membrane supported Ag NWs filtrate and curing at 90 °C for 1 h. After removing the PTFE membrane, the Ag electrode was obtained in the form of a Ag NWs-PDMS matrix layer. The AZ electrode was then fabricated by first pouring PDMS on the Ag electrode, followed by placing the AZ BHS (attached to PTFE membrane) on top, and curing the PDMS at 90 °C for 1 h. After the PDMS has cured, the PTFE membrane was removed, leaving a partially encapsulated and exposed AZ BHS layer, which was then sulfurized via the above-mentioned procedure.

Measurement of Piezoelectric Output. Electrical contacts were made by attaching wires to the device with conductive Ag paste, and the device was connected to the Keithley 4200-SCS machine to measure the piezoelectric voltage output. Ultrasonic actuation was carried out with an ultrasonic bath (Fisherbrand FB15051, 37 kHz).

PEC Measurement (Water Splitting and Methyl Orange Degradation). Two × 1 cm AZ and Ag/Ag_2S-ZnO/ZnS (ASZS) active electrodes were tested in a two-electrode PEC configuration with Pt foil as the counter electrode in an aqueous 25 mM anhydrous sodium sulfate (Na_2SO_4) electrolyte. The setup was illuminated, and the photocurrents were measured using a potentiostat (Princeton Applied Research, Parstat 4000). PEC degradation of MO was investigated by adding aqueous MO solution (0.4 mM) with 0.1 mL of H_2O_2 into the electrolyte.

Materials Characterization. The morphology of the BHS was characterized with a SEM (JEOL FEG JSM 7001F) operated at 15 kV. The elements present in the nanostructures were analyzed using energy-dispersive X-ray spectroscopy (EDX, Oxford Instruments), and the valence states of the various elements were determined through XPS. The crystalline structures and elemental compositions of the BHS were analyzed using XRD (D5005 Bruker X-ray diffractometer equipped with graphite-monochromated Cu Kα radiation at λ = 1.541 Å), TEM,) and STEM (JEOL 2100 TEM). Absorption spectra of the samples were measured with a UV−vis-NIR spectrophotometer (UV−vis, Shimadzu UV-3600). A Keithley 4200-SCS semiconductor characterization system was used to study the piezoelectric voltage output from the BHS. The amount of H_2 gas produced from the photocatalytic experiments was measured by gas chromatography (Shimadzu GC2010 TCD). The photocurrent from the PEC cell was measured using a potentiostat (Princeton Applied Research, Parstat 4000).

Conflict of Interest: The authors declare no competing financial interest.

Supporting Information Available: SEM images of silver nanowires and copper nanowires and ASZS and CSZS. TEM images, XPS, and XRD spectra of ASZS and CSZS BHS. UV−vis absorbance of AZ, CZ, ASZS, and CSZS BHS. Elemental mapping of ZS NRs from ASZS BHS. The Supporting Information is available free of charge on the ACS Publications website at DOI: 10.1021/acsnano.5b03075.

Acknowledgment. This work is supported by the A*STAR grant R-263-000-A96-305 and MOE R-263-000-B38-112/R-263-000-B63-112.

REFERENCES AND NOTES

1. Xu, C.; Wang, X. D.; Wang, Z. L. Nanowire Structured Hybrid Cell for Concurrently Scavenging Solar and Mechanical Energies. *J. Am. Chem. Soc.* **2009**, *131*, 5866–5872.
2. Xu, C.; Wang, Z. L. Compact Hybrid Cell Based on a Convoluted Nanowire Structure for Harvesting Solar and Mechanical Energy. *Adv. Mater.* **2011**, *23*, 873–877.
3. Yang, Y.; Zhang, H. L.; Lin, Z. H.; Liu, Y.; Chen, J.; Lin, Z. Y.; Zhou, Y. S.; Wong, C. P.; Wang, Z. L. A Hybrid Energy Cell for Self-Powered Water Splitting. *Energy Environ. Sci.* **2013**, *6*, 2429–2434.
4. Yoon, G. C.; Shin, K.-S.; Gupta, M. K.; Lee, K. Y.; Lee, J.-H.; Wang, Z. L.; Kim, S.-W. High-Performance Hybrid Cell Based on an Organic Photovoltaic Device and a Direct Current Piezoelectric Nanogenerator. *Nano Energy* **2015**, *12*, 547–555.
5. Wang, X. D. Piezoelectric Nanogenerators-Harvesting Ambient Mechanical Energy at the Nanometer Scale. *Nano Energy* **2012**, *1*, 13–24.
6. Fujishima, A.; Honda, K. Electrochemical Photolysis of Water at a Semiconductor Electrode. *Nature* **1972**, *238*, 37–38.
7. Roundy, S.; Wright, P. K. A Piezoelectric Vibration Based Generator for Wireless Electronics. *Smart Mater. Struct.* **2004**, *13*, 1131–1142.
8. Cha, S. N.; Seo, J. S.; Kim, S. M.; Kim, H. J.; Park, Y. J.; Kim, S. W.; Kim, J. M. Sound-Driven Piezoelectric Nanowire-Based Nanogenerators. *Adv. Mater.* **2010**, *22*, 4726–4730.
9. Lee, S.; Bae, S. H.; Lin, L.; Yang, Y.; Park, C.; Kim, S. W.; Cha, S. N.; Kim, H.; Park, Y. J.; Wang, Z. L. Super-Flexible Nanogenerator for Energy Harvesting From Gentle Wind and as an Active Deformation Sensor. *Adv. Funct. Mater.* **2013**, *23*, 2445–2449.

10. Zhong Lin, W. *Nanogenerators for Self-Powered Devices and Systems*; Georgia Institute of Technology: Atlanta, GA, 2011.
11. Yang, P. K.; Lin, Z. H.; Pradel, K. C.; Lin, L.; Li, X. H.; Wen, X. N.; He, J. H.; Wang, Z. L. Paper-Based Origami Triboelectric Nanogenerators and Self-Powered Pressure Sensors. *ACS Nano* **2015**, *9*, 901–907.
12. Sohn, J. I.; Cha, S. N.; Song, B. G.; Lee, S.; Kim, S. M.; Ku, J.; Kim, H. J.; Park, Y. J.; Choi, B. L.; Wang, Z. L.; et al. Engineering of Efficiency Limiting Free Carriers and an Interfacial Energy Barrier for an Enhancing Piezoelectric Generation. *Energy Environ. Sci.* **2013**, *6*, 97–104.
13. Lee, S.; Lee, J.; Ko, W.; Cha, S.; Sohn, J.; Kim, J.; Park, J.; Park, Y.; Hong, J. Solution-Processed Ag-Doped ZnO Nanowires Grown on Flexible Polyester for Nanogenerator Applications. *Nanoscale* **2013**, *5*, 9609–9614.
14. Liu, R.; Zheng, Z.; Spurgeon, J.; Yang, X. G. Enhanced Photoelectrochemical Water-Splitting Performance of Semiconductors by Surface Passivation Layers. *Energy Environ. Sci.* **2014**, *7*, 2504–2517.
15. Wang, M. Y.; Sun, L.; Lin, Z. Q.; Cai, J. H.; Xie, K. P.; Lin, C. J. P-N Heterojunction Photoelectrodes Composed of Cu_2O-Loaded TiO_2 Nanotube Arrays with Enhanced Photoelectrochemical and Photoelectrocatalytic Activities. *Energy Environ. Sci.* **2013**, *6*, 1211–1220.
16. Ye, M. D.; Gong, J. J.; Lai, Y. K.; Lin, C. J.; Lin, Z. Q. High-Efficiency Photoelectrocatalytic Hydrogen Generation Enabled by Palladium Quantum Dots-Sensitized TiO_2 Nanotube Arrays. *J. Am. Chem. Soc.* **2012**, *134*, 15720–15723.
17. Wang, H.-P.; Sun, K.; Noh, S. Y.; Kargar, A.; Tsai, M.-L.; Huang, M.-Y.; Wang, D.; He, J.-H. High-Performance a-Si/c-Si Heterojunction Photoelectrodes for Photoelectrochemical Oxygen and Hydrogen Evolution. *Nano Lett.* **2015**, *15*, 2817–2824.
18. Kudo, A.; Miseki, Y. Heterogeneous Photocatalyst Materials for Water Splitting. *Chem. Soc. Rev.* **2009**, *38*, 253–278.
19. Hong, K.-S.; Xu, H.; Konishi, H.; Li, X. Direct Water Splitting Through Vibrating Piezoelectric Microfibers in Water. *J. Phys. Chem. Lett.* **2010**, *1*, 997–1002.
20. Ong, W. L.; Yew, K. W.; Tan, C. F.; Adrian, T. K. T.; Hong, M. H.; Ho, G. W. Highly Flexible Solution Processable Heterostructured Zinc Oxide Nanowires Mesh for Environmental Clean-Up Applications. *RSC Adv.* **2014**, *4*, 27481–27487.
21. Wang, M. Y.; Ioccozia, J.; Sun, L.; Lin, C. J.; Lin, Z. Q. Inorganic-Modified Semiconductor TiO_2 Nanotube Arrays for Photocatalysis. *Energy Environ. Sci.* **2014**, *7*, 2182–2202.
22. Xue, X.; Zang, W.; Deng, P.; Wang, Q.; Xing, L.; Zhang, Y.; Wang, Z. L. Piezo-Potential Enhanced Photocatalytic Degradation of Organic Dye Using ZnO Nanowires. *Nano Energy* **2015**, *13*, 414–422.
23. Hu, Y. F.; Zhang, Y.; Xu, C.; Zhu, G. A.; Wang, Z. L. High-Output Nanogenerator by Rational Unipolar Assembly of Conical Nanowires and its Application for Driving a Small Liquid Crystal Display. *Nano Lett.* **2010**, *10*, 5025–5031.
24. Hu, Y. F.; Xu, C.; Zhang, Y.; Lin, L.; Snyder, R. L.; Wang, Z. L. A Nanogenerator for Energy Harvesting from A Rotating Tire and its Application as a Self-Powered Pressure/Speed Sensor. *Adv. Mater.* **2011**, *23*, 4068–4071.
25. Yang, R.; Qin, Y.; Li, C.; Zhu, G.; Wang, Z. L. Converting Biomechanical Energy into Electricity by a Muscle-Movement-Driven Nanogenerator. *Nano Lett.* **2009**, *9*, 1201–1205.
26. Kim, K. H.; Lee, K. Y.; Seo, J. S.; Kumar, B.; Kim, S. W. Paper-Based Piezoelectric Nanogenerators with High Thermal Stability. *Small* **2011**, *7*, 2577–2580.
27. Kumar, B.; Kim, S. W. Recent Advances in Power Generation Through Piezoelectric Nanogenerators. *J. Mater. Chem.* **2011**, *21*, 18946–18958.
28. Lee, K. Y.; Gupta, M. K.; Kim, S.-W. Transparent Flexible Stretchable Piezoelectric and Triboelectric Nanogenerators for Powering Portable Electronics. *Nano Energy* **2015**, *14*, 139–160.
29. He, J. H.; Hsin, C. L.; Liu, J.; Chen, L. J.; Wang, Z. L. Piezoelectric Gated Diode of a Single ZnO Nanowire. *Adv. Mater.* **2007**, *19*, 781–784.
30. Kumar, B.; Kim, S. W. Energy Harvesting Based on Semiconducting Piezoelectric ZnO Nanostructures. *Nano Energy* **2012**, *1*, 342–355.
31. Hernandez, S.; Hidalgo, D.; Sacco, A.; Chiodoni, A.; Lamberti, A.; Cauda, V.; Tresso, E.; Saracco, G. Comparison of Photocatalytic and Transport Properties Of TiO_2 And ZnO Nanostructures for Solar-Driven Water Splitting. *Phys. Chem. Chem. Phys.* **2015**, *17*, 7775–7786.
32. Zhang, J. Y.; Wang, Y. H.; Zhang, J.; Lin, Z.; Huang, F.; Yu, J. G. Enhanced Photocatalytic Hydrogen Production Activities of Au-Loaded ZnS Flowers. *ACS Appl. Mater. Interfaces* **2013**, *5*, 1031–1037.
33. Xu, F.; Shen, Y. T.; Sun, L. T.; Zeng, H. B.; Lu, Y. N. Enhanced Photocatalytic Activity of Hierarchical ZnO Nanoplate-Nanowire Architecture as Environmentally Safe and Facilely Recyclable Photocatalyst. *Nanoscale* **2011**, *3*, 5020–5025.
34. Sun, Y. G.; Mayers, B.; Herricks, T.; Xia, Y. N. Polyol Synthesis of Uniform Silver Nanowires: A Plausible Growth Mechanism and the Supporting Evidence. *Nano Lett.* **2003**, *3*, 955–960.
35. Jin, M. S.; He, G. N.; Zhang, H.; Zeng, J.; Xie, Z. X.; Xia, Y. N. Shape-Controlled Synthesis of Copper Nanocrystals in an Aqueous Solution with Glucose as a Reducing Agent and Hexadecylamine as a Capping Agent. *Angew. Chem., Int. Ed.* **2011**, *50*, 10560–10564.
36. Zheng, Z. K.; Lim, Z. S.; Peng, Y.; You, L.; Chen, L.; Wang, J. L. General Route to ZnO Nanorod Arrays on Conducting Substrates *via* Galvanic-Cell-Based Approach. *Sci. Rep.* **2013**, *3*, 2434.
37. Lu, M.-Y.; Song, J.; Lu, M.-P.; Lee, C.-Y.; Chen, L.-J.; Wang, Z. L. ZnO−ZnS Heterojunction and ZnS Nanowire Arrays for Electricity Generation. *ACS Nano* **2009**, *3*, 357–362.
38. Kushwaha, A.; Aslam, M. ZnS Shielded ZnO Nanowire Photoanodes for Efficient Water Splitting. *Electrochim. Acta* **2014**, *130*, 222–231.
39. Fan, W. G.; Jewell, S.; She, Y. Y.; Leung, M. K. H. *In Situ* Deposition of Ag-Ag_2S Hybrid Nanoparticles onto TiO_2 Nanotube Arrays towards Fabrication of Photoelectrodes with High Visible Light Photoelectrochemical Properties. *Phys. Chem. Chem. Phys.* **2014**, *16*, 676–680.
40. Bar, M.; Ennaoui, A.; Klaer, J.; Kropp, T.; Saez-Araoz, R.; Allsop, N.; Lauermann, I.; Schock, H. W.; Lux-Steiner, M. C. Formation of a ZnS/Zn(S,O) Bilayer Buffer on $CuInS_2$ Thin Film Solar Cell Absorbers by Chemical Bath Deposition. *J. Appl. Phys.* **2006**, *99*, 123503.
41. Gogurla, N.; Sinha, A. K.; Santra, S.; Manna, S.; Ray, S. K. Multifunctional Au-Zno Plasmonic Nanostructures for Enhanced UV Photodetector and Room Temperature NO Sensing Devices. *Sci. Rep.* **2014**, *4*, 6483.
42. Gholami, M.; Qorbani, M.; Moradlou, O.; Naseri, N.; Moshfegh, A. Z. Optimal Ag_2S Nanoparticle Incorporated TiO_2 Nanotube Array for Visible Water Splitting. *RSC Adv.* **2014**, *4*, 7838–7844.
43. Mansour, A. N. Copper Mg Kα XPS Spectra From the Physical Electronics Model 5400 Spectrometer. *Surf. Sci. Spectra* **1994**, *3*, 202–210.
44. Perry, D. L.; Taylor, J. A. X-Ray Photoelectron and Auger Spectroscopic Studies of Cu_2S and CuS. *J. Mater. Sci. Lett.* **1986**, *5*, 384–386.
45. Bhide, V. G.; Salkalachen, S.; Rastogi, A. C.; Rao, C. N. R.; Hegde, M. S. Depth Profile Composition Studies of Thin-Film CdS-Cu_2S Solar-Cells using XPS and AES. *J. Phys. D: Appl. Phys.* **1981**, *14*, 1647–1656.
46. Herrmann, J. M.; Tahiri, H.; Aitichou, Y.; Lassaletta, G.; Gonzalezelipe, A. R.; Fernandez, A. Characterization and Photocatalytic Activity in Aqueous Medium of TiO_2 and Ag-TiO_2 Coatings on Quartz. *Appl. Catal., B* **1997**, *13*, 219–228.
47. Zhu, T.; Peh, C. K. N.; Hong, M. H.; Ho, G. W. Outside-In Recrystallization of ZnS-$Cu_{1.8}S$ Hollow Spheres with Interdispersed Lattices for Enhanced Visible Light Solar Hydrogen Generation. *Chem. - Eur. J.* **2014**, *20*, 11505–11510.
48. Zhu, T.; Zhang, C.; Ho, G. W. *In Situ* Dissolution-Diffusion Toward Homogeneous Multiphase Ag/Ag_2S@Zns Core-Shell

Heterostructures for Enhanced Photocatalytic Performance. *J. Phys. Chem. C* **2015**, *119*, 1667–1675.
49. Zhao, H.; Dong, Y.; Jiang, P.; Wu, X.; Wu, R.; Chen, Y. Facile Preparation of a ZnS/ZnO Nanocomposite for Robust Sunlight Photocatalytic H_2 Evolution from Water. *RSC Adv.* **2015**, *5*, 6494–6500.
50. Kaneko, M.; Okura, I. *Photocatalysis: Science And Technology*; Springer-Verlag: Berlin, Germany, 2002.
51. Xu, S.; Hansen, B. J.; Wang, Z. L. Piezoelectric-Nanowire-Enabled Power Source for Driving Wireless Microelectronics. *Nat. Commun.* **2010**, *1*, 93.
52. Floro, J. A.; Michael, J. R.; Brewer, L. N.; Hsu, J. W. P. Preferred Heteroepitaxial Orientations of ZnO Nanorods on Ag. *J. Mater. Res.* **2010**, *25*, 1352–1361.
53. Dongre, J. K.; Nogriya, V.; Aloney, R.; Ramrakhiani, M. Nanostructures Based Photoelectrochemical Cells for Energy Conversion. *Optoelectron. Adv. Mater.* **2009**, *3*, 338–342.
54. Zainal, Z.; Lee, C. Y.; Kassim, A.; Hussein, M. Z.; Yusof, N. A. Photoelectrochemical Degradation of Methyl Orange using TiO_2/Ti Films Prepared *via* Sol-Gel Technique. *Acta Chim. Slov.* **2007**, *54*, 166–174.
55. Shen, Y. M.; Li, F.; Li, S. F.; Liu, D. B.; Fan, L. H.; Zhang, Y. Electrochemically Enhanced Photocatalytic Degradation of Organic Pollutant on Beta-PbO_2-TNT/Ti/TNT Bifuctional Electrode. *Int. J. Electrochem. Sci.* **2012**, *7*, 8702–8712.
56. Kevin, M.; Lim, G. Y. R.; Ho, G. W. Facile Control of Copper Nanowire Dimensions *via* the Maillard Reaction: Using Food Chemistry for Fabricating Large-Scale Transparent Flexible Conductors. *Green Chem.* **2015**, *17*, 1120–1126.